Investigating Early-Stage Au Nucleation on Graphene via Grand-Canonical DFT and Machine-Learned Interatomic Potentials

Gianluca A. O. Seaford[1, 2] and Nicholas D. M. Hine[2]

[1)]School of Engineering, University of Warwick, Coventry, CV4 7AL, United Kingdom

[2)]Department of Physics, University of Warwick, Coventry, CV4 7AL, United Kingdom

(*Electronic mail: Luca.Seaford@warwick.ac.uk)

(Dated: 23 October 2025)

Developing *in silico* simulations of highly charged electrochemical interfaces is vital for understanding and modelling the early stages of nucleation. We employ grand-canonical ensemble DFT (GC-eDFT) in ONETEP to compute potential-dependent adsorption and single-atom nucleation free energies, and to extract the Au reservoir chemical potential μ_{Au}, for Au adatoms on Bernal-stacked graphene under vacuum-jellium and implicit solvent-electrolyte environments at -0.10, 0.00, and $+0.10$ V. Adsorption curves versus height are shallow and near-parallel across hollow/top/bridge sites, consistent with physisorption and low site selectivity; solvation uniformly stabilises the adsorbate, making $\mu_{Au} \sim 1.3$ eV more negative than in vacuum at fixed bias. Asymptotic tail fits favour a dominant non-retarded Casimir-Polder dispersion term with a minor weak-retardation correction and yield $\mu_{Au}(V) \approx \mu_0 + sV$ with slopes $s = 10.97$ and 12.75 eV V^{-1} in vacuum and solution, respectively. Nucleation is mildly exergonic in vacuum with minima near $3.0 - 3.4$ Å; in solution, nucleation free energies are more height-dependent, with endergonic behaviour at small h and exergonic behaviour at larger separations, reflecting dielectric/ionic screening.

I. INTRODUCTION

Metallic nanoclusters on graphene and graphene-like substrates underpin a wide range of technologies, from biosensing and drug delivery to catalysis and energy storage[1–3]. Among these, gold (Au) clusters supported on graphene offer unique electronic and catalytic properties, enabling applications such as fuel-cell catalysts and biosensors[4]. The earliest stages of nucleation are governed by adsorption–diffusion dynamics, which strongly influence nanoparticle morphology and thus functional performance. However, these mechanisms are not fully understood. Experimental techniques, including liquid-phase transmission electron microscopy (TEM) as outlined in Fig.1(a), lack the temporal resolution to observe such dynamics[5,6], while conventional electronic-structure methods struggle with the charge-transfer effects and electrochemical conditions intrinsic to electrode–electrolyte interfaces[7].

Simulating such systems in silico presents real challenges. Conventional density functional theory (DFT) approaches are formulated within the canonical ensemble, fixing the number of electrons within the system a priori. This prevents fine control over applied bias and, by extension, the electrochemical potential. Furthermore, the cubic scaling associated with operations on the eigenstates of the Kohn–Sham (KS) Hamiltonian makes fully quantum-mechanical simulations of explicitly solvated interfaces prohibitively expensive[8]. Hybrid quantum–continuum models address some of these challenges by replacing explicit solvent with an implicit dielectric and introducing ionic screening through a Poisson–Boltzmann (PB) description[9–11]. Yet, accurate modelling under potential control requires extending DFT formalism to the grand-canonical ensemble.

This limitation on conventional DFT has motivated the development of grand-canonical DFT approaches, which allows the electronic chemical potential to be fixed, and thus provides a suitable framework for simulating bias-dependent processes at electrochemical interfaces[12–14]. These advances have enabled realistic modelling of electrochemical systems without resorting to jellium charge compensation or ad hoc background corrections, which can lead to artefacts in screening behaviour[15]. Other workarounds—such as external sawtooth fileds[16], surface dipole corrections[17], or countercharge planes[18]—have also been used to impose an effective bias, but they require system-specific tuning and can distort interfacial electrostatics[17,19].

However, the computational cost of grand-canonical ensemble calculations remains substantial, even within a linear scaling framework. This makes systematic exploration of adsorption sites and the ab-initio construction of potential-dependent free-energy landscapes impractical, particularly for nucleation studies. This is due to the requirement for multiple cluster sizes, forces, and applied potentials to understand the dynamics governing the early stages of nucleation of adatoms[20,21].

This work aims to address these challenges laying the foundations needed to combine the grand-canonical ensemble-DFT (GC-eDFT) framework outlined by Bhandari *et al.*[14] in the ONETEP[22,23] linear scaling DFT code with modern machine learning techniques[24]. The potential-control methodology, introduced by Bhandari and co-workers for Li nucleation on graphite[21], is adapted to investigate the early stages of Au nucleation on a graphene bilayer. The potential-dependent grand-canonical free energies in the presence of an implicit Poisson–Boltzmann electrolyte are calculated, and used to extract the adsorption and nucleation free-energies for Au adatoms as a thermodynamic descriptor as a precursor for training multi-head grand-canonical MACE (GC-MACE) surrogates[24,25], providing a scalable route to mapping free-energy landscapes for electrochemical nucleation.

II. THEORY

A. System

When modelling complex interfacial systems, one typically treats the problem either fully quantum-mechanically, or using some form of hybrid quantum-continuum model[26]. The former requires a fully quantum representation of the solvent and electrolyte, in addition to the surface considered, and thus becomes computationally intractable for even moderately sized systems. The latter replaces the explicit solvent-electrolyte component with some continuum model, treating only the core surface with a full quantum description, improving tractability.

The total charge density $\rho_{tot}(\mathbf{r})$ within the system can be expressed as the sum of charge densities from the quantum subsystem ρ_q, and from the mobile continuum electrolyte ρ_{mob}. The quantum charge density can be further broken down into electronic and nuclear contributions, denoted by ρ_e and ρ_{nuc} respectively. Hence the total charge density is:

$$\rho_{tot}(\mathbf{r}) = \rho_e(\mathbf{r}) + \rho_{nuc}(\mathbf{r}) + \underbrace{\sum_i^p z_i c_i(\mathbf{r})}_{\rho_{mob}}, \qquad (1)$$

where z_i and $c_i(\mathbf{r})$ denote the charge and concentration of ion i respectively.

For this work, we focus solely on the adsorption–reduction half-reaction describing the nucleation of Au adatoms onto the graphene bilayer

$$n \cdot Au^{3+}(\text{sol.}) + 3n \cdot e^- \rightarrow Au_n | G . \qquad (2)$$
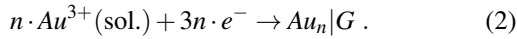
To model such systems in silico, we replace the traditional in situ liquid TEM setup depicted in Fig.1(a) with a system typically found in electrochemistry; two electrodes surrounded by some solvation environment Fig.1(b,c). One electrode, typically referred to as the control or reference electrode, is treated implicitly while the other electrode is simulated within the hybrid quantum-continuum framework.

B. Grand-Canonical Free-Energy Functional

When considering DFT in the grand-canonical ensemble, one must use the natural thermodynamic potential: the finite-temperature grand-canonical free-energy Ω_ϑ. For our system one can separate this functional into three distinct components: the grand-potential of electrons Ω_e; the mean-field electrostatic functional Ω_{mf}; and a non-mean-field interaction term Ω_{nmf}.

The electronic component Ω_e is the Legendre transform of the finite-temperature Helmholtz free-energy F_ϑ, as given by Eq.6

$$\Omega_e[\rho_e, c_i, v] := F_\vartheta[\rho_e] - \mu_e \cdot N_e. \qquad (3)$$

Here v, μ_e and N_e denote the

The mean-field electrostatic functional Ω_{mf} contains contributions from the electrostatic and electrolytic repulsion energy, osmotic pressure, electrolyte entropy, and electrolyte chemical potential. A full overview of the mathematical framework for this functional can be found in the works by Bhandari et al.[14] and Dziedzic et al.[11]. The non-mean-field correction Ω_{nmf} incorporates the cavitation, dispersion and repulsion effects that are not captured using mean-field theory. This is taken to be proportional to the accessible surface area of the solvent, and is outlined in[27,28]. Together these terms account for both local and long-range screening effects induced by the electrolyte.

Minimising the free-energy functional with respect to the electrolyte concentrations $c_i(\mathbf{r})$ and the total electrostatic potential $v(\mathbf{r})$ yields a Poisson-Boltzmann (PB) equation:

$$\nabla \cdot [\varepsilon(\mathbf{r})\nabla v(\mathbf{r})] = -4\pi \left[\rho_e(\mathbf{r}) + \rho_{nuc}(\mathbf{r}) + \sum_i^p z_i c_i(\mathbf{r}) \right], \quad (4)$$

which is solved iteratively for each inner loop iteration in the GC-eDFT minimisation, as outlined in section II D, to ensure charge neutrality within the system.

C. ONETEP

Traditional plane-wave DFT implementations[29,30] work directly with eigenstates of the Kohn–Sham (KS) Hamiltonian. While a natural and highly effective framework for investigating electronic structure, it suffers from a fundamental limitation: computational overheads scale cubically with system size.

Linear-scaling (LS) DFT codes[22,23,31,32] bypass this constraint by working directly with the density matrix ρ rather than the more natural KS eigenstates. ONETEP[22,23] achieves linear scaling via the construction of a set of, in general non-orthogonal, localised orbitals $\{\varphi_\alpha\}$ called non-orthogonal generalised Wannier functions (NGWFs), effectively capturing the inherent 'locality' of many-body quantum systems. KS orbitals $\{\psi_i\}$ can be recovered via a linear transformation of the aforementioned NGWFs.

The density matrix ρ can then be expressed in terms of these NGWFs as

$$\rho(\mathbf{r}, \mathbf{r}') = \varphi_\alpha(\mathbf{r}) K^{\alpha\beta} \varphi_\beta(\mathbf{r}'). \qquad (5)$$

Here, $K^{\alpha\beta}$ denotes the density kernel; the representation of the density matrix in the NGWF basis. This kernel encodes both the occupancy numbers of the KS orbitals and the couplings between NGWFs, and its sparsity is vital to ensuring linear scaling.

Controllable accuracy equivalent to plane-wave pseudopotential calculations is achieved by expanding the NGWFs using a periodic sinc (p-sinc) basis, effectively bandwidth-limited delta distributions, across some grid $\{\mathbf{r}_i\}$. These p-sinc functions are controlled by enforcing $c_{i\alpha} = 0$ outside a strict cutoff radius. Grid point spacing is controlled via a plane-wave-equivalent energy cutoff E_{cut}, thus providing
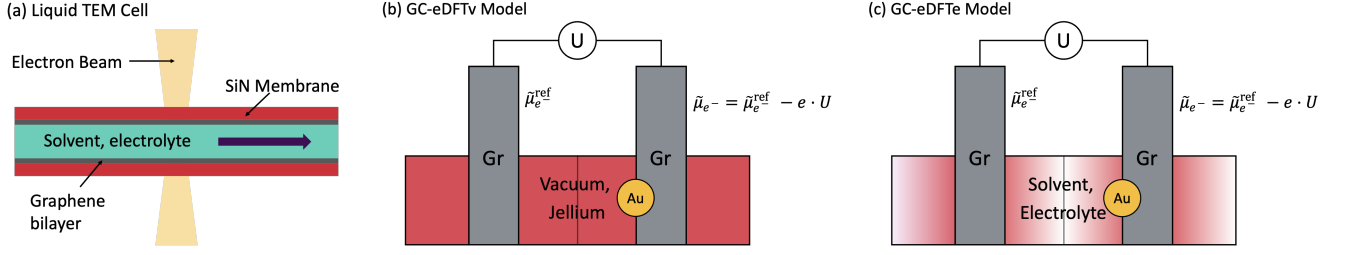
FIG. 1. (a) A cross-section diagram of a third-generation liquid transmission electron microscopy (TEM) cell used for in situ material studies. (b-c) Schematics of the grand-canonical ensemble-DFT (GC-eDFT) system in ONETEP for the vacuum-jellium (GC-eDFTv) and the solvent-electrolyte (GC-eDFTe) systems respectively.

controllable accuracy that approaches that of plane-wave formalisms asymptotically.

1. Projector Augmented Wave

The projector augmented wave (PAW) approach outlined by Blöchl[33] combines the efficiency and transferability of plane-wave pseudopotential methodologies with the accuracy of all-electron (AE) calculations. This is achieved by relating the soft pseudopotential (PS) wavefunctions to rapidly-oscillating AE wavefunctions via a linear transformation, allowing for more efficient treatments of elements that are difficult for norm-conserving pseudopotentials.

Since ONETEP does not have direct access to the eigenstates of the KS Hamiltonian, the fundamental PAW equation must be reformulated in terms of the AE and PS density matrices in the NGWF basis[34]. Consequently, the mathematical framework is modified with the overlap matrix, Hamiltonian matrix elements, NGWF gradients, and force expressions being redefined to incorporate the PAW transformation. For a full overview of the mathematics behind this implementation, readers are directed to[34].

In this work, PAW is particularly important for accurately describing Au, whose semi-core 5d states, valence 6s states, and relativistic effects pose challenges for norm-conserving pseudopotentials. Using PAW within ONETEP therefore ensures reliable adsorption energetics and charge transfer within the solvated Au–graphene system.

2. Canonical and Grand-Canonical Ensemble-DFT

Ensemble-DFT (eDFT) expands the KS formalism to allow for each KS state ψ_i to have fractional occupancies. These occupancies are regulated using a constant electronic temperature ϑ, and calculated according to the Fermi-Dirac distribution. This removes the idempotency constraint on the density kernel, enabling a finite-temperature Helmholtz free-energy functional to be defined in terms of the NGWFs $\{\varphi_\alpha\}$ and density kernel $\mathbf{K}$:

$$F_\vartheta\left[\{\varphi_\alpha\}, \mathbf{K}\right] = E\left[\{\varphi_\alpha\}, \mathbf{K}\right]$$
$$+ k_B \vartheta \text{Tr}\left[\mathbf{K}\log\left[\mathbf{K}\right] + (\hat{\mathbf{1}} - \mathbf{K})\log\left[\hat{\mathbf{1}} - \mathbf{K}\right]\right]. \quad (6)$$

Here, the first term is the KS ground-state energy functional and second term is the standard entropic correction from the non-interacting electronic system. This functional, once the occupational equilibrium is attained, has stationary points equivalent to solutions of the KS eigenvalue problem for fractional occupancies[35].

ONETEP minimises F_ϑ via a two-level nested optimisation scheme[36,37]. The outer loop optimises the NGWFs, while the inner loop optimises the Hamiltonian using a Pulay-style method[38] subject to a constraint on the number of electrons in the system[23,39]. Although the diagonalisation step scales cubically, the localisation of the NGWF basis ensures the Hamiltonian matrix remains sparse, keeping the computational overhead low.

In the GC-eDFT framework, the Helmholtz free-energy functional F_ϑ is replaced by the electronic component of the finite-temperature grand free-energy functional $\Omega_e = F_\vartheta - \mu_e \cdot N_e$. Unlike canonical eDFT, the number of electrons is not fixed; instead, the electronic chemical potential $\tilde{\mu}_e$ is fixed via the use of an applied electrochemical bias U. This applied bias sets the system electronic chemical potential via $\tilde{\mu}_e = \mu_e^{\text{ref}} - e \cdot U$.

The variational form of the NGWF gradients can be shown to be invariant under the change in ensemble, and thus the same two-level nested optimisation scheme can be applied with minimal modification: the Hamiltonian diagonalisation routine is subject to a fixed $\tilde{\mu}_e$ rather than a fixed number of electrons.

D. Charge Neutralisation

As in all DFT calculations, care must be taken to ensure charge is neutralised within the system to prevent spurious Coulombic interactions between periodic images. This requirement becomes particularly important in electrochemical systems, where highly charged interfaces are common. To address this, ONETEP employs the neutralisation by electrolyte concentration shift (NECS) method introduced by Bhandari et al.[40], which generalises earlier approaches by Gunceler et al.[10] and Melander et al.[12] to complex electrochemical environments. This framework adjusts electrolyte concentrations in response to solute charge, thereby mimicking the charge transfer that occurs naturally under open boundary conditions

(OBCs).

When imposing periodic boundary constraints (PBCs) it is more natural to shift ionic concentrations than to impose ad hoc uniform background charges, which can distort screening behaviour[40]. In NECS, the local electrolyte density is modified according to a Boltzmann-like distribution, with an additional potential shift term that ensures overall charge neutrality.

The electrostatic potential $v(\mathbf{r})$ is determined at each self-consistent field (SCF) iteration by solving the non-linear Poisson–Boltzmann equation with the DL_MG solver[41]; a parallel library optimised for solving the full PB equation. The resulting electrolyte concentrations are then updated via NECS and fed back into the Hamiltonian prior to diagonalisation, ensuring charge neutrality is enforced consistently throughout the minimisation of the electronic free-energy functional.

E. Nucleation Energies

Building on the half-reaction introduced in Section II A, the thermodynamics of Au nucleation can be evaluated via the potential-dependent adsorption free energies within the GC-eDFT framework. For a cluster of size n, the nucleation grand free energy $\Delta\Omega_\vartheta(U)$ at applied bias U is given by:

$$\Delta\Omega_\vartheta(U) := \Omega_{\vartheta,\mathrm{Au}_n|_G}(U) - \Omega_{\vartheta,G}(U) - n \cdot \mu_{\mathrm{Au}}^{\mathrm{ref}}, \quad (7)$$

where $\Omega_{\vartheta,\mathrm{Au}_n|_G}(U)$ and $\Omega_{\vartheta,G}(U)$ denote the total grand free-energy of the adsorbed Au cluster of size n at the graphene substrate and the clean graphene substrate respectively. Here, $\mu_{\mathrm{Au}}^{\mathrm{ref}}$ is the reference electrochemical potential of Au. This measures the balance between the stabilisation gained by adsorption, the cost of drawing atoms from the Au reservoir, and the influence of the applied potential, which sets the electronic chemical potential.

This formulation mirrors the role of the Gibbs free-energy in classical nucleation theory (CNT), where the nucleation barrier arises from the competition between a bulk driving force and a surface energy penalty. In the present framework, $\Delta\Omega_\vartheta(U)$ plays the role of this free-energy profile, with the applied potential shifting the balance of terms. In practice, the evaluation of $\Delta\Omega_\vartheta(U)$ for small cluster sizes provides direct insight into the earliest stages of electrochemical nucleation, enabling insights from a region not accessible by CNT.

III. COMPUTATIONAL METHODOLOGY

We employed the GC-eDFT functionality of ONETEP[14] with the optB88-vdW functional[42] at $\vartheta = 298.15$ K to simulate Au nucleation on graphene. Two models were considered: a vacuum-jellium system (GC-eDFTv) with uniform background neutralisation, and a solvent-electrolyte system (GC-eDFTe) where charge was balanced using the NECS scheme[40]. The systems comprised a $6 \times 6 \times 2$ Bernal-stacked graphene bilayer with Au adatoms placed at high-symmetry sites, subject to applied potentials of -0.10, 0.00, and +0.10 V

relative to the graphene reference electrode. Core electrons were treated with JTH_PBE PAW pseudopotentials, with NGWF radii of 10.0 Bohr (C) and 12.0 Bohr (Au). A plane-wave equivalent cutoff of 750 eV was used, with Brillouin-zone sampling performed using a $4 \times 4 \times 1$ Monkhorst-Pack grid.

In GC-eDFTe, a 0.1 M HAuCl$_4$ electrolyte, comprising H$^+$ and [AuCl$_4$]$^-$ ions, was employed. A steric smearing width of 0.8 Bohr was applied, and solvation radii of 3.1 Bohr (C) and 3.2 Bohr (Au) were used. Solvation was treated using the auto-solvation routine[27], with a soft-sphere dielectric of $\varepsilon = 78.4$ and surface tension 0.072 N/m, consistent with liquid water at room temperature. The electrostatic potential was solved self-consistently at each SCF step using the DL_MG Poisson–Boltzmann solver[41].

A. Uncertainty Quantification

1. Jackknife

Uncertainty estimates for the Dirac energy E_D were calculated using a block jackknife approach[43,44]. For each system, environment, bias triple, we first calculated E_D using a local quadratic fit to the Density of States (DoS) in the vicinity of the minimum. The sensitivity was investigated by partitioning the quadratic fit into n disjoint intervals of equal length before applying a delete-one-block jackknife. The standard error is then

$$\sigma_{\mathrm{jackknife}} = \sqrt{\frac{n-1}{n} \sum_{i=1}^{n} \left[(E_D)_i - \bar{E}_D \right]^2}, \quad (8)$$

where $\bar{E}_D$ denotes the mean of the delete-one-block refits. The uncertainty in the solvation shift ΔE was calculated using a simple quadrature rule for combining uncertainties.

One must note that this method provides an uncertainty in the extraction of E_D from the DoS plots, and does not quantify the global uncertainty arising from the selection of parameters like the exchange-correlation functional, k-point mesh, pseudopotentials or plane-wave equivalent cutoff energy. Such uncertainty quantification is beyond the scope of this paper.

IV. RESULTS AND DISCUSSION

A. Graphene Reference Chemical Potential ($\tilde{\mu}_{\mathrm{Gr}}^{\mathrm{ref}}$)

Since in situ liquid TEM cells consist of two thin, parallel multilayer graphene plates separated by a channel in which our solvent flows, we require the chemical potential of our graphene bilayer reference electrode to act as a baseline for all GC-eDFT calculations. To calculate a suitable chemical potential, $\tilde{\mu}_{\mathrm{Gr}}^{\mathrm{ref}}$, for the graphene reference electrode, one considers a relaxed Bernal-stacked graphene bilayer in an implicit 0.1M $AuCl_4^-$ solution in a water solvent. An e-DFT single-point calculation for the system was performed at temperature $\vartheta = 298.15$ K to obtain the Fermi level. This Fermi level,

once converted from Hartree to eV, serves as a natural reference electrochemical potential. From this simulation, one obtains an electronic Fermi level -2.70 eV. Since all subsequent GC-eDFT calculations were performed using this Fermi level as the reference chemical potential $\tilde{\mu}_e^{\text{ref}}$, calculations will be referred to by the applied potential, and not the electronic chemical potential $\tilde{\mu}_e$.

B. Gold Chemical Potential $(\tilde{\mu}_{\mathbf{Au}})$

In order to evaluate nucleation energies, one requires a suitable chemical potential for the adsorbate atom; the third term in Eq.7. Obtaining this chemical potential, however, is computationally expensive. Typical approaches, like that employed by Bhandari *et al.*[14], perform large-scale (GC-)DFT calculations using a fine k-point mesh on large bulk-like systems to obtain a suitable chemical potential. This is problematic for early-stage investigations in two ways: small clusters tend to prefer Archimedean, Platonic or Catalan solids[45] over bulk-like arrangements; and performing the large-scale GC-eDFT computations in vacuo and in solution becomes prohibitively expensive.

To avoid calculating an ab-inito bulk-Au GC-eDFT reference, we determine the Au chemical potential μ_{Au} by extrapolating the large-separation tail of the adsorption free energy. For a neutral adsorbate above a 2D surface, like the graphene bilayer, the leading non-retarded dispersion has $\Delta\Omega_{\text{ads}}(h) \sim \mu_{\text{Au}} + C_3/h^3$[46,47]. In practice, short-range Pauli repulsion can leak into the "tail" at the largest separations we can sample, and small retardation effects may also appear[48]. We therefore fit an augmented asymptotic form

$$\Delta\Omega_{\text{ads}}(h) \approx \mu_{\text{Au}} + \frac{C_3}{h^3} + \frac{C_4}{h^4} + Ae^{-\alpha h} + B\frac{e^{-\kappa h}}{h}, \quad (9)$$

and extract μ_{Au} for each environment and bias. Here, the $1/h^3$ term captures the non-retarded Casimir-Polder limit[46,49]; long-range adsorbate-surface interactions arising from the electromagnetic field[50]. The $1/h^4$ term captures weak retardation effects[46]; while $Ae^{-\alpha h}$ accounts for residual overlap[48]. The final term, capturing screened image-charge effects due to the imposed periodic boundary conditions, is only required if the Au cluster has non-neutral charge.

We perform weighted least squares that emphasises the largest available heights, with corresponding weights $w \propto [(h - h_{\min})/(h_{\max} - h_{\min})]^\gamma$. The exponential rates α and κ are scanned over a small grid; for any (α, κ) tuple, the model is linear in parameters $\{\mu, C_3, C_4, A, B\}$, and is thus solved analytically.

Among all candidates, the model with the lowest (weighted) Akaike information criterion (AIC)[51,52], a metric that balances model complexity against the quality of the fit, was selected. The fitted μ_{Au} is then used for calculations of the nucleation energy.

Focusing first on model selection (Table I), the AIC consistently favours the simplest augmented tail, $\mu + C_3/h^3 + C_4/h^4$. This points to a dominant non-retarded dispersion term, C_3/h^3, with a small weak-retardation correction. The

TABLE I. Calculated μ_{Au} from Eq.9 sorted by environment and bias.

Environment	Bias	μ_{Au}(eV)	AIC_w	R_w^2
Vacuum-Jellium	-0.10 V	-900.733	-177.87	0.152
Vacuum-Jellium	$+0.00$ V	-899.439	-180.16	0.495
Vacuum-Jellium	$+0.10$ V	-898.540	-172.31	0.118
Solvent-Electrolyte	-0.10 V	-902.071	-160.93	0.731
Solvent-Electrolyte	$+0.00$ V	-900.909	-162.97	0.777
Solvent-Electrolyte	$+0.10$ V	-899.520	-157.89	0.702

residual-overlap term $Ae^{-\alpha h}$ and the screened-image term $Be^{-\kappa h}/h$ were not selected by AIC, indicating that our largest separations already lie in a weak-overlap regime and that any charge-induced image contribution is negligible over the sampled bias window; adding these parameters does not improve the weighted AIC enough to justify the extra complexity.

The quality of the large-h tail fit is markedly better in solution: R_w^2 lies between 0.70 and 0.78 for the solvated series, versus 0.12–0.50 in vacuum, consistent with dielectric/ionic screening attenuating long-range electrostatic perturbations and yielding a cleaner asymptotic regime. At fixed bias, the solvated μ_{Au} is 0.98–1.47 eV more negative than in vacuum (mean ≈ 1.3 eV), reflecting stabilisation by the PB electrolyte.

The fitted μ_{Au} becomes less negative with increasing bias, displaying a near-linear dependence on V. A simple least-squares fit across the three biases yields $d\mu/dV\big|_{\text{vac}} = 10.97$ eV V^{-1} and $d\mu/dV\big|_{\text{sol}} = 12.75$ eV V^{-1}, corresponding to shifts of ~ 2.19 eV and ~ 2.55 eV across the applied bias range, in excellent agreement with Table I.

In this region, we can thus write $\mu_{\text{Au}}(V) \approx \mu_0 + sV$ and define an effective electron-number response $\Delta N_{\text{eff}} \approx \partial\mu/\partial V$, to the applied bias U giving $\Delta N_{\text{eff}} \approx 11$ and ≈ 13 for the vacuum and solvated systems respectively. This indicates that the Au cluster effectively exchanges around 11–13 electrons per volt with the electronic reservoir, with solvation increasing its charge-response capacity.

C. Density of States

Densities of states were computed from ONETEP eigenvalues using k-point weights and Gaussian broadening with $\sigma = 0.10$ eV on a 2000-point energy grid spanning $[-10, +10]$ eV. All energies are reported relative to each calculation's Fermi level.

Focusing first on the 'Dirac' points, one notices that the linear dispersive relation obeyed by the π-manifold in the graphene monolayer is replaced by an approximately parabolic relation in the graphene bilayer. In the density of states (DoS) this point appears as a shallow local minimum of finite, but non-zero, density. The Dirac energy E_D, defined as the energy corresponding to the Dirac minimum nearest E_F, is obtained from a quadratic fit. By convention $E_D < 0$ indicates E_F lies above the Dirac minimum (n-type) and $E_D > 0$ indicates it lies below (p-type).

In the DoS overlays (Fig.2), clean graphene (Au-000; panels a–b) shows the expected shallow minimum within the
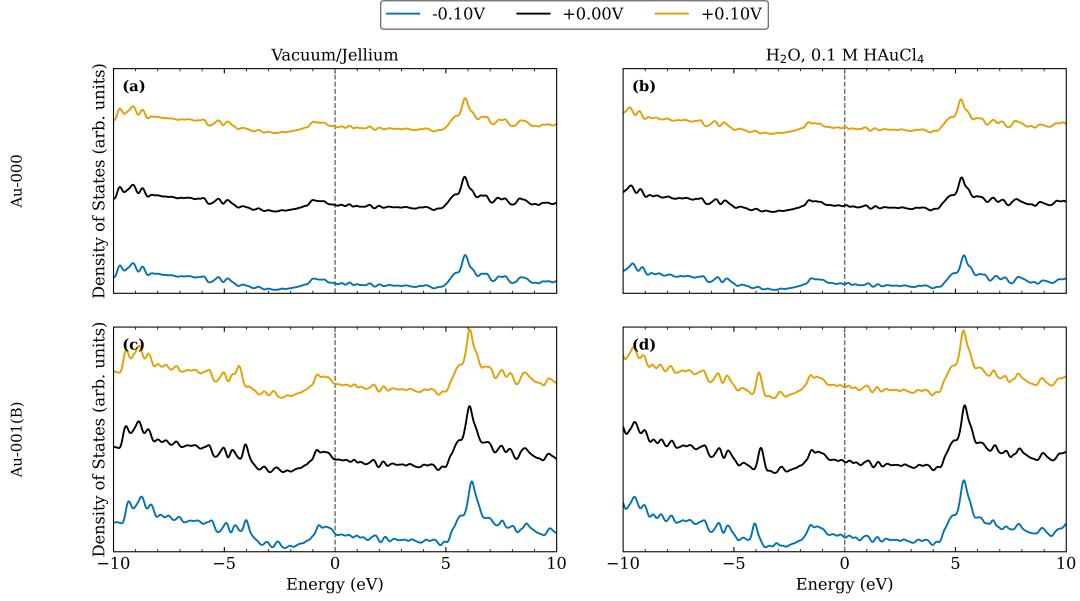
FIG. 2. Density of states (DoS) plots for the clean graphene bilayer (top) and the bilayer with an adsorbed Au atom (bottom). (a,b) Density of states (DoS) plots for the clean graphene bilayer in the vacuum-jellium (a) and solvent-electrolyte (b) environments respectively. (c,d) Density of states (DoS) plots for the graphene bilayer with an additional Au adatom located at a bridge site in the vacuum-jellium (c) and solvent-electrolyte (d) environments respectively. The applied biases $+0.1$V, $+0.0$V and -0.1V are plotted in orange, black and blue respectively.

Dirac region, within a smooth π-manifold background that gently rises into a broad maximum on the unoccupied side (about $+5$–6 eV). Moving from vacuum to the solvated environment, this minimum becomes noticeably deeper and narrower and the background around E_F tightens; the three bias traces shift almost in parallel, indicating a near-rigid response to the ± 0.10 V applied bias, in contrast to the solvation or adatom effects.

In the adatom case (Au-001(B); panels c–d), additional structure appears: resonances at positive energies and shoulders on the occupied side, consistent with π–Au hybridisation that introduces extra spectral weight near E_F and increases asymmetry. Solvation suppresses the broad background, sharpens the near-E_F region, and accentuates the minimum relative to vacuum. Spectral features, like the strong unoccupied peak near $+5$–6 eV, remain at similar energies with only minor bias-dependent offsets.

Considering the Dirac energy, one observes a clear negative shift between the vacuum and solvated environments. For clean graphene (Au-000) the shift is modest and bias-dependent, with observed shifts between -0.29 and $-0.60 eV$. The introduction of an Au adatom generates greater shifts in the Dirac energy; typically between -0.7 and $-1.0 eV$ for the T site, and up to $-1.36 eV$ for the B site at -0.10 V, while the H site ranges from -0.34 eV at -0.10 V to -1.22 eV at $+0.10$ V. These trends are consistent with electrolyte screening that sharpens the near-E_F DoS and stabilises the minimum, while adatom–graphene hybridisation modifies the π manifold and brings additional spectral weight toward E_F.

Using the jackknife approach outlined in Sec.III A 1, we find systematically smaller uncertainties for the solvated sys-

tems ~ 0.03 to ~ 0.29 eV at 2σ, consistent with electrolyte screening. In contrast, several vacuum calculations of the adsorbed system carry very large uncertainties. For example, the H and B sites have $2\sigma \approx 1.3$ eV, reflecting shallow or multi-minimum structure in the Dirac region under vacuum in which the quadratic fit can migrate between nearby dips under k-block resampling. Cases where E_D sits very close to E_F, like the vacuum calculation of pure graphene with a $+0.10$ V applied bias, should likewise be read cautiously, since the estimator becomes sensitive to small changes in smoothing or fit window.

D. Adsorption ($\Delta\Omega_{\text{ads}}$) & Nucleation Free-Energy ($\Delta\Omega_\vartheta$)

The nucleation energy ($\Delta\Omega_\vartheta$) given by Eq.7 gives a quantitative representation of the thermodynamic feasibility for nucleation to occur. Focusing on the adsorption contribution first, we plot the difference in free-energy between the adsorbed system and the pristine graphene bilayer as a function of the adatom height h, corresponding to the first two terms of Eq.7. This is given by Fig.3. Mapping $\Delta\Omega_{\text{ads}}(h)$ serves two purposes. First, it reveals whether the sampled height range reaches the large-separation tail needed to extract a reservoir chemical potential μ_{Au}. Second, it disentangles environmental effects from the choice of adsorption site, providing insight into which factor dominates the energetics.

Across all three high-symmetry sites, $\Delta\Omega_{\text{ads}}(h)$ only varies weakly over the selected height range. This shallow, near-parallel behaviour is characteristic of physisorption on graphene. The lack of clear site-dependent minima implies

TABLE II. A table of the 'Dirac' energies E_D of the bilayer system computed from the density of states (DoS), measured relative to the Fermi level E_F, with corresponding 2σ uncertainties obtained via a leave-one-k jackknife over the DoS estimate of E_D. The energy shift $\Delta E_D = E_D^{\rm rel,\,solv} - E_D^{\rm rel,\,vac}$ uses a quadrature combination of the per-environment 2σ uncertainties.

| System	Bias	$E_D^{\rm rel,\,vac}$ (eV)	$E_D^{\rm rel,\,solv}$ (eV)	ΔE_D (eV)
Au-000	-0.10V	-0.3109 ± 0.0450	-0.6047 ± 0.0300	-0.2938 ± 0.0541
Au-000	$+0.00$V	-0.3061 ± 0.0450	-0.6035 ± 0.0300	-0.2974 ± 0.0541
Au-000	$+0.10$V	-0.0031 ± 0.0450	-0.6063 ± 0.0300	-0.6032 ± 0.0541
Au-001(H)	-0.10V	-0.3652 ± 1.2880	-0.7087 ± 0.2655	-0.3435 ± 1.3151
Au-001(H)	$+0.00$V	-0.3670 ± 1.2994	-0.5559 ± 0.2805	-0.1889 ± 1.3293
Au-001(H)	$+0.10$V	0.3009 ± 0.3713	-0.9192 ± 0.2305	-1.2201 ± 0.4370
Au-001(T)	-0.10V	0.2944 ± 0.3925	-0.7095 ± 0.2755	-1.0039 ± 0.4795
Au-001(T)	$+0.00$V	0.2234 ± 0.3655	-0.5038 ± 0.2101	-0.7272 ± 0.4216
Au-001(T)	$+0.10$V	0.2827 ± 0.3925	-0.5583 ± 0.2851	-0.8410 ± 0.4851
Au-001(B)	-0.10V	0.2914 ± 0.3925	-1.0702 ± 0.2006	-1.3616 ± 0.4408
Au-001(B)	$+0.00$V	-0.3465 ± 1.2807	-0.5092 ± 0.2056	-0.1627 ± 1.2971
Au-001(B)	$+0.10$V	0.3137 ± 0.3713	-0.5068 ± 0.2156	-0.8205 ± 0.4294
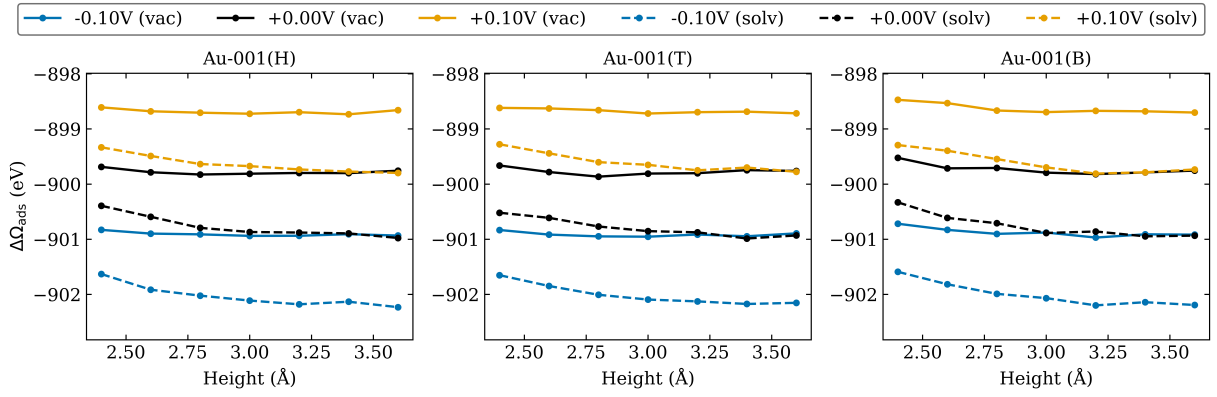
FIG. 3. Adsorption free-energy curves for an Au adatom located at the (a) Hollow (b) Top and (c) Bridge high-symmetry sites for the vacuum-jellium (solid) and solvent-electrolyte (dashed) systems. The $+0.10$V, $+0.00$V and -0.10V applied biases are shown in orange, black and blue respectively.

that geometry only plays a minor role in determining adsorption energetics. At larger adatom heights, one notices a plateau behaviour, implying the system enters a region where long-range dispersive effects dominate. In this region, changes in the applied bias produce near-vertical offsets, with minimal change to the underlying curvature, supporting the use of the long-tail scheme to estimate $\mu_{\rm Au}$ as outlined in Sec.IV B.

Focusing on the effects of the solvation environment, one observes a clear shift between the vacuum-jellium (solid) and solvent-electrolyte (dashed) systems, with the solvent-electrolyte series sitting below the vacuum-jellium series. The increasing divergence between the two solvation environments in the large h limit, consistent with the dielectric screening stabilising the adsorbed cluster within the solvent-electrolyte system.

The relative flatness of the adsorption energy landscape—a consequence of the structural properties of graphene—suggests a mobile Au adatom with low migration barriers and weak site selectivity. Hence, nucleation tendencies are more likely to be governed by global factors, like the

solvation environment and applied biases, rather than by more subtle geometric differences between adsorption sites.

Shifting focus to the nucleation energies, shown in Fig.4, we plot the nucleation free-energy $\Delta\Omega_\vartheta$ as a function of the adatom height. Here, more-negative free-energies imply nucleation is more thermodynamically favourable.

Across all sites, the curves display a stronger height dependence for the solvent-electrolyte (dashed) system than the vacuum-jellium (solid) system. In the vacuum systems, one observes a mildly exergonic $\Delta\Omega_\vartheta$, corresponding to an environment favourable to nucleation, with free-energy minima in the region of $3.0 - 3.4$ Å with corresponding magnitudes on the order of a few tenths of an eV.

In contrast, the solvent–electrolyte series (dashed) display a stronger height dependence: $\Delta\Omega_\vartheta$ is often endergonic at small separations ($h \lesssim 2.6$ Å) and crosses into the exergonic regime only beyond ~ 3 Å. This is most likely due to the electrolyte screening penalising adatoms close to the surface through a cavitation/polarisation cost, while stabilising the weakly bound, dispersion-dominated adatom at larger separations. Differences between adsorption sites are modest, typ-
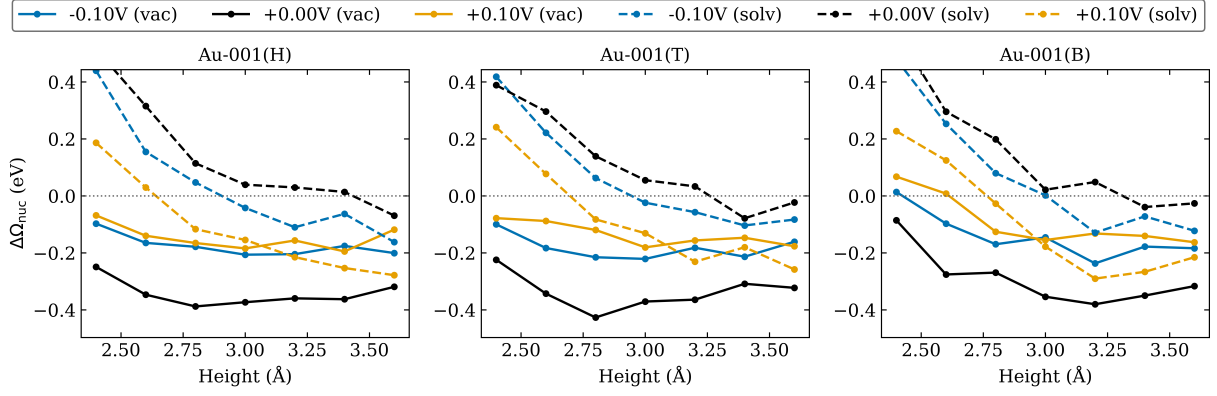
FIG. 4. Nucleation free-energy curves for an Au adatom located at the (a) Hollow (b) Top and (c) Bridge high-symmetry sites for the vacuum-jellium (solid) and solvent-electrolyte (dashed) systems. The $+0.10$V, $+0.00$V and -0.10V applied biases are shown in orange, black and blue respectively.

ically $\lesssim 0.1 - 0.2$ eV. Overall, single-atom nucleation is thermodynamically accessible across a broad height window, suggesting that kinetics (rather than thermodynamics) will likely control early growth.

Within a given environment the bias series are separated, but not dramatically so. This is expected given how the current curves were constructed; the reservoir chemical potential μ_{Au} was fitted separately for each applied bias and subtracted in forming $\Delta\Omega_{\vartheta}$. Using the bias-specific μ_{Au} largely cancels the uniform bias-driven offset, leaving only the residual bias response of the adsorption free-energy. As a result, the pronounced near-vertical shifts anticipated due to the applied bias are muted.

This oversight will need to be corrected in later drafts of this work, using instead the μ_{Au} calculated for the system under zero bias. This provides a common reference for calculating $\Delta\Omega_{\vartheta}$, and allows the bias-dependent shifts to be observed. These shifts can be predicted using the values of $d\mu_{Au}/dV$ calculated in Sec. IV A), with rigid bias-dependent offsets of order $|d\mu_{Au}/dV| \cdot \Delta V$.

To place all nucleation free-energy curves on a common reference, we re-express $\Delta\Omega_{\vartheta}$ using the zero-bias Au reservoir, $\mu_0 \equiv \mu_{Au}(V{=}0)$, rather than the bias-specific $\mu_{Au}(V)$ used in Fig.4.

Given $\mu(V) \approx \mu_0 + sV$, the corrected nucleation energy is a rigid offset of the plotted values, and is given by

$$\Delta\Omega_{\vartheta}^{corr}(V) = \Delta\Omega_{\vartheta}^{old}(V) + n_{Au} \cdot \frac{\partial\mu_{Au}}{\partial V} V. \qquad (10)$$

Corrections calculated using Eq.10 can be found in Tab.III. Applying these corrections results in the nucleation curves at positive and negative biases being translated up and down respectively by ~ 1.10 eV for the vacuum system and by ~ 1.28 eV for the solvated system.

TABLE III. Corrections to the nucleation free-energies calculated using Eq.10 from data in Tab.I.

Bias	Vacuum Correction (eV)	Solvent Correction (eV)
-0.10 V	-1.097	-1.275
$+0.00$ V	$+0.000$	$+0.000$
$+0.10$ V	$+1.097$	$+1.275$

V. CONCLUSIONS & FUTURE WORK

We have established a consistent grand-canonical DFT (GC-eDFT) workflow for bias-controlled adsorption and single-atom nucleation of Au on Bernal-stacked graphene, comparing vacuum-jellium and implicit solvent–electrolyte environments at -0.10, 0.00 and $+0.10$ V. Mapping $\Delta\Omega_{ads}(h)$ across hollow, top and bridge registries shows shallow, near-parallel height dependences characteristic of physisorption, with weak site selectivity. Large-separation tails are well described by $\mu + C_3/h^3 + C_4/h^4$, indicating dominant non-retarded dispersion with a minor weak-retardation correction; overlap and screened-image terms are not required by AIC. Tail fits yield Au reservoir chemical potentials that are ~ 1.3 eV more negative in solution than in vacuum at fixed bias, consistent with dielectric/ionic stabilisation, and exhibit a near-linear bias response with slopes of 10.97 and 12.75 eV V^{-1} in vacuum and solution, respectively.

Nucleation free-energy profiles $\Delta\Omega_{\vartheta}(h)$ are mildly exergonic in vacuum with minima near $3.0 - 3.4$ Å, whereas in solution they are more height-dependent—often endergonic at short range and exergonic at larger separations—reflecting electrolyte screening. Differences between high-symmetry sites are modest ($\lesssim 0.1 - 0.2$ eV), suggesting that environment and potential, rather than geometric registry, dominate the early thermodynamics. We note a methodological caveat: using bias-specific $\mu_{Au}(V)$ in the nucleation definition largely cancels the rigid, bias-driven offsets. We therefore provide simple, linear corrections to $\Delta\Omega_{\vartheta}$ to account for the bias-dependent μ_{Au} (see Table III) that translate the curves by

± 1.097 eV (vacuum) and ± 1.275 eV (solution) at ± 0.10 V, restoring the expected potential-dependent shifts.

Three immediate extensions follow from the present study. The first focuses on re-expressing all nucleation curves using a common zero-bias reservoir, $\mu_{Au}(0)$, rather than $\mu_{Au}(V)$, to expose the rigid potential-dependent offsets predicted by $\partial \mu_{Au}/\partial V$. This correction will be applied uniformly across sites and environments, after which the potential of zero nucleation energy (PZNE), the applied potential for which $\Delta\Omega_\vartheta(V) = 0$, will be calculated. Mapping the PZNE across sites and, subsequently, cluster sizes will provide a compact thermodynamic descriptor for bias-controlled nucleation.

Next, we will focus on training fast surrogate models to enable broader exploration of early-stage nucleation. Two complementary routes will be pursued: a custom multi-head MACE MLIP trained on GC-eDFT data with distinct heads for each applied bias; and fine-tuning the MACE-MP0 foundation model using multi-head replay learning to prevent catastrophic forgetting. Uncertainty-aware committees will be used, with the calculated variance used to trigger additional data generation in an active-learning framework. Additional GC-eDFT calculations will be trained on structures generated using stochastic-MD, enabling models to be used for dynamical simulations.

Finally, we aim to incorporate electron-beam effects relevant to in situ liquid TEM by treating the beam as a localised stochastic energy source that perturbs atomic motion. These effects will be modelled by incorporating Poisson-timed velocity 'kicks' that inject additional kinetic energy into the system. Kick directions will be sampled uniformly on the unit sphere, while magnitudes will be drawn from a narrow distribution calibrated to match a desired dose-equivalent target, while net linear momentum is zeroed at each kick to prevent drift. A weak Langevin or some spatially inhomogeneous thermostat will dissipate injected energy over some timescale, establishing a stationary non-equilibrium state. Free parameters, like electrolyte concentration and applied potentials, will be tuned to closely match experiments performed by our experimental collaborators. Representative snapshots will then be used for GC-eDFT calculations to obtain the free-energy for MLIP training. If needed, additional terms accounting for electrostatic charging and radiolysis may be introduced.

ACKNOWLEDGMENTS

DATA AVAILABILITY STATEMENT

All processed data underlying the figures, together with version-controlled analysis scripts, are available in a GitHub repository, https://github.com/G-Seaford/HetSys-Peer-UQ.git, which will be made public upon acceptance. To facilitate reproducibility without rerunning GC-eDFT, we provide a minimal, self-contained workflow that reproduces the Dirac-energy shift for the clean graphene (Au-000) and adsorbed system (Au-001(T)) at -0.10, 0.00, and $+0.10$ V applied biases for both the vacuum-jellium and solvent–electrolyte environments. This repository includes the per-block density-of-states inputs, a single Python script that computes E_D via a local quadratic fit with a delete-one-block jackknife UQ scheme (reporting 2σ uncertainties), a short *README* with step-by-step instructions, and a *requirements.txt* specifying package versions.

In addition, the repository contains the scripts used to generate adsorption-tail fits and μ_{Au} values from the supplied CSV files, along with selected ONETEP input decks and key output logs for completeness. Owing to size and licensing constraints, only GC-eDFT inputs, outputs, and simulation logs are deposited; further files are available from the corresponding author on reasonable request.

[1] B. F. Machado and P. Serp, **2**, 54.

[2] A. Ambrosi, C. K. Chua, A. Bonanni, and M. Pumera, **114**, 7150.

[3] M. B. Burkholder, F. B. A. Rahman, E. H. Chandler, J. R. Regalbuto, B. F. Gupton, and J. M. M. Tengco, **9**, 100196.

[4] K. Turcheniuk, R. Boukherroub, and S. Szunerits, **3**, 4301.

[5] J. Park, K. Koo, N. Noh, J. H. Chang, J. Y. Cheong, K. S. Dae, J. S. Park, S. Ji, I.-D. Kim, and J. M. Yuk, **15**, 288.

[6] N. de Jonge and F. M. Ross, **6**, 695.

[7] S. Ringe, N. G. Hörmann, H. Oberhofer, and K. Reuter, **122**, 10777.

[8] S. Goedecker, **71**, 1085.

[9] R. Jinnouchi and A. B. Anderson, **77**, 245417.

[10] D. Gunceler, K. Letchworth-Weaver, R. Sundararaman, K. A. Schwarz, and T. A. Arias, **21**, 074005.

[11] J. Dziedzic, A. Bhandari, L. Anton, C. Peng, J. C. Womack, M. Famili, D. Kramer, and C.-K. Skylaris, **124**, 7860.

[12] M. M. Melander, M. J. Kuisma, T. E. K. Christensen, and K. Honkala, **150**, 041706.

[13] K. Mathew, V. S. C. Kolluru, S. Mula, S. N. Steinmann, and R. G. Hennig, **151**, 234101.

[14] A. Bhandari, C. Peng, J. Dziedzic, L. Anton, J. R. Owen, D. Kramer, and C.-K. Skylaris, **155**, 024114 (2021).

[15] G. Kastlunger, P. Lindgren, and A. A. Peterson, **122**, 12771.

[16] J. Neugebauer and M. Scheffler, **46**, 16067.

[17] C. Freysoldt, A. Mishra, M. Ashton, and J. Neugebauer, **102**, 045403, publisher: American Physical Society.

[18] M. Otani and O. Sugino, **73**, 115407.

[19] M. J. Rutter, **3**, 015002.

[20] B. Scharifker and G. Hills, **28**, 879.

[21] A. Bhandari, C. Peng, J. Dziedzic, J. R. Owen, D. Kramer, and C.-K. Skylaris, **10**, 11426 (2022).

[22] C.-K. Skylaris, P. D. Haynes, A. A. Mostofi, and M. C. Payne, **122**, 084119.

[23] J. C. A. Prentice, J. Aarons, J. C. Womack, A. E. A. Allen, L. Andrinopoulos, L. Anton, R. A. Bell, A. Bhandari, G. A. Bramley, R. J. Charlton, R. J. Clements, D. J. Cole, G. Constantinescu, F. Corsetti, S. M.-M. Dubois, K. K. B. Duff, J. M. Escartín, A. Greco, Q. Hill, L. P. Lee, E. Linscott, D. D. O'Regan, M. J. S. Phipps, L. E. Ratcliff, R. Serrano, E. W. Tait, G. Teobaldi, V. Vitale, N. Yeung, T. J. Zuehlsdorff, J. Dziedzic, P. D. Haynes, N. D. M. Hine, A. A. Mostofi, M. C. Payne, and C.-K. Skylaris, **152**, 174111 (2020).

[24] I. Batatia, D. P. Kovács, G. N. C. Simm, C. Ortner, and G. Csányi, arXiv (2023), 10.48550/arXiv.2206.07697, 2206.07697.

[25] I. Batatia, P. Benner, Y. Chiang, A. M. Elena, D. P. Kovács, J. Riebesell, X. R. Advincula, M. Asta, M. Avaylon, W. J. Baldwin, F. Berger, N. Bernstein, A. Bhowmik, S. M. Blau, V. Cărare, J. P. Darby, S. De, F. D. Pia, V. L. Deringer, R. Elijošius, Z. El-Machachi, F. Falcioni, E. Fako, A. C. Ferrari, A. Genreith-Schriever, J. George, R. E. A. Goodall, C. P. Grey, P. Grigorev, S. Han, W. Handley, H. H. Heenen, K. Hermansson, C. Holm, J. Jaafar, S. Hofmann, K. S. Jakob, H. Jung, V. Kapil, A. D. Kaplan, N. Karimitari, J. R. Kermode, N. Kroupa, J. Kullgren, M. C. Kuner, D. Kuryla, G. Liepuoniute, J. T. Margraf, I.-B. Magdău, A. Michaelides, J. H. Moore, A. A. Naik, S. P. Niblett, S. W. Norwood, N. O'Neill, C. Ortner, K. A. Persson, K. Reuter, A. S. Rosen, L. L. Schaaf, C. Schran, B. X. Shi, E. Sivonxay, T. K. Stenczel, V. Svahn, C. Sutton, T. D. Swinburne, J. Tilly, C. v. d. Oord, E. Varga-Umbrich, T. Vegge, M. Vondrák, Y. Wang, W. C. Witt, F. Zills, and G. Csányi, arXiv (2024), 10.48550/arXiv.2401.00096, 2401.00096.

[26] O. Andreussi, I. Dabo, and N. Marzari, **136**, 064102.

[27] J. Dziedzic, H. H. Helal, C.-K. Skylaris, A. A. Mostofi, and M. C. Payne, **95**, 43001 (2011).

[28] J. Dziedzic, S. J. Fox, T. Fox, C. S. Tautermann, and C.-K. Skylaris, **113**, 771 (2013).

[29] X. Gonze, B. Amadon, G. Antonius, F. Arnardi, L. Baguet, J.-M. Beuken, J. Bieder, F. Bottin, J. Bouchet, E. Bousquet, N. Brouwer, F. Bruneval, G. Brunin, T. Cavignac, J.-B. Charraud, W. Chen, M. Côté, S. Cottenier, J. Denier, G. Geneste, P. Ghosez, M. Giantomassi, Y. Gillet, O. Gingras, D. R. Hamann, G. Hautier, X. He, N. Helbig, N. Holzwarth, Y. Jia, F. Jollet, W. Lafargue-Dit-Hauret, K. Lejaeghere, M. A. L. Marques, A. Martin, C. Martins, H. P. C. Miranda, F. Naccarato, K. Persson, G. Petretto, V. Planes, Y. Pouillon, S. Prokhorenko, F. Ricci, G.-M. Rignanese, A. H. Romero, M. M. Schmitt, M. Torrent, M. J. van Setten, B. Van Troeye, M. J. Verstraete, G. Zérah, and J. W. Zwanziger, **248**, 107042.

[30] J. J. Mortensen, A. H. Larsen, M. Kuisma, A. V. Ivanov, A. Taghizadeh, A. Peterson, A. Haldar, A. O. Dohn, C. Schäfer, E. Jónsson, E. D. Hermes, F. A. Nilsson, G. Kastlunger, G. Levi, H. Jónsson, H. Häkkinen, J. Fojt, J. Kangsabanik, J. Sødequist, J. Lehtomäki, J. Heske, J. Enkovaara, K. T. Winther, M. Dulak, M. M. Melander, M. Ovesen, M. Louhivuori, M. Walter, M. Gjerding, O. Lopez-Acevedo, P. Erhart, R. Warmbier, R. Würdemann, S. Kaappa, S. Latini, T. M. Boland, T. Bligaard, T. Skovhus, T. Susi, T. Maxson, T. Rossi, X. Chen, Y. L. A. Schmerwitz, J. Schiøtz, T. Olsen, K. W. Jacobsen, and K. S. Thygesen, **160**, 092503.

[31] M. J. Gillan, D. R. Bowler, A. S. Torralba, and T. Miyazaki, Proceedings of the Conference on Computational Physics 2006, **177**, 14.

[32] S. Mohr, L. E. Ratcliff, L. Genovese, D. Caliste, P. Boulanger, S. Goedecker, and T. Deutsch, **17**, 31360.

[33] P. E. Blöchl, **50**, 17953.

[34] N. D. M. Hine, **29**, 024001.

[35] B. I. Halperin, **175**, 521.

[36] N. Marzari, D. Vanderbilt, and M. C. Payne, **79**, 1337.

[37] Ruiz-Serrano and C.-K. Skylaris, **139**, 054107.

[38] N. D. Woods, M. C. Payne, and P. J. Hasnip, **31**, 453001.

[39] C. Freysoldt, S. Boeck, and J. Neugebauer, **79**, 241103.

[40] A. Bhandari, L. Anton, J. Dziedzic, C. Peng, D. Kramer, and C.-K. Skylaris, **153**, 124101.

[41] J. C. Womack, L. Anton, J. Dziedzic, P. J. Hasnip, M. I. J. Probert, and C.-K. Skylaris, **14**, 1412.

[42] J. Klimeš, D. R. Bowler, and A. Michaelides, **22**, 022201.

[43] M. H. QUENOUILLE, **43**, 353.

[44] J. Jiang, P. Lahiri, and S.-M. Wan, **30**, 1782.

[45] T. Mori and T. Hegmann, **18**, 295.

[46] H. B. G. Casimir and D. Polder, **73**, 360.

[47] E. Zaremba and W. Kohn, **13**, 2270.

[48] J. N. Israelachvili, *Intermolecular and surface forces*, 3rd ed. (Academic Press).

[49] M. Bordag, **96**, 062504, publisher: American Physical Society.

[50] E. A. Power, **22**, 453.

[51] H. Akaike, **19**, 716.

[52] C. M. Hurvich and C.-L. Tsai, **76**, 297.